

# Core Mass Estimates in Strong Lensing Galaxy Clusters: a Comparison Between Masses Obtained from Detailed Lens Models, Single-Halo Lens Models, and Einstein Radii

J. D. REMOLINA GONZÁLEZ,<sup>1</sup> K. SHARON,<sup>1</sup> G. MAHLER,<sup>1,2,3</sup> C. FOX,<sup>1</sup> C.A. GARCIA DIAZ,<sup>4</sup> K. NAPIER,<sup>1</sup> L. E. BLEEM,<sup>5,6</sup>  
M. D. GLADDERS,<sup>7,6</sup> N. LI,<sup>8,9</sup> AND A. NIEMIEC<sup>1,2,3</sup>

<sup>1</sup>*Department of Astronomy, University of Michigan, 1085 S. University Ave, Ann Arbor, MI 48109, USA*

<sup>2</sup>*Centre for Extragalactic Astronomy, Department of Physics, Durham University, Durham DH1 3LE, UK*

<sup>3</sup>*Institute for Computational Cosmology, Durham University, South Road, Durham DH1 3LE, UK*

<sup>4</sup>*Division of Physics, Engineering, Mathematics, and Computer Science, Delaware State University, 1200 N. Dupont Hwy, Dover, DE, United States*

<sup>5</sup>*Argonne National Laboratory, High-Energy Physics Division, Argonne, IL 60439*

<sup>6</sup>*Kavli Institute for Cosmological Physics, University of Chicago, 5640 South Ellis Avenue, Chicago, IL 60637, USA*

<sup>7</sup>*Department of Astronomy and Astrophysics, University of Chicago, 5640 South Ellis Avenue, Chicago, IL 60637, USA*

<sup>8</sup>*CAS, Key Laboratory of Space Astronomy and Technology, National Astronomical Observatories, A20 Datun Road, Chaoyang District, Beijing 100012, People's Republic of China*

<sup>9</sup>*School of Physics and Astronomy, Nottingham University, University Park, Nottingham NG7 2RD, UK*

Submitted to ApJ

## ABSTRACT

The core mass of galaxy clusters is both an important anchor of the radial mass distribution profile and probe of structure formation. With thousands of strong lensing galaxy clusters being discovered by current and upcoming surveys, timely, efficient, and accurate core mass estimates are needed. We assess the results of two efficient methods to estimate the core mass of strong lensing clusters: the mass enclosed by the Einstein radius ( $M_{\text{corr}}(< \theta_E)$ ; Remolina González et al. 2020), and single-halo lens model ( $M_{\text{SHM}}(< e\theta_E)$ ; Remolina González et al. 2021), against measurements from publicly available detailed lens models ( $M_{\text{DLM}}$ ) of the same clusters. We use publicly available lens models from the Sloan Giant Arc Survey, the Reionization Lensing Cluster Survey, the *Hubble* Frontier Fields, and the Cluster Lensing and Supernova Survey with *Hubble*. We find a scatter of 18.3% (8.4%) with a bias of  $-7.5\%$  (0.4%) between  $M_{\text{corr}}(< \theta_E)$  ( $M_{\text{SHM}}(< e\theta_E)$ ) and  $M_{\text{DLM}}$ . Last, we compare the statistical uncertainties measured in this work to those from simulations. This work demonstrates the successful application of these methods to observational data. As the effort to efficiently model the mass distribution of strong lensing galaxy clusters continues, we are in need of fast and reliable methods to advance the field.

**Keywords:** Galaxies: Clusters: General - Gravitational Lensing: Strong - Cosmology: Dark Matter

## 1. INTRODUCTION

Galaxy clusters are harbored at the knots of the cosmic web and trace the large-scale structure of the universe, making them ideal cosmic laboratories (see reviews by Allen et al. 2011 and Mantz et al. 2014). The galaxy cluster mass function connects the underlying cosmology and the observational properties of galaxy clusters (e.g., Evrard et al. 2002; Pratt et al. 2019; Boc-

quet et al. 2020). Additional predictions from cosmological simulations include the radial mass distribution of dark matter halos (e.g., Duffy et al. 2008; Meneghetti et al. 2014; Child et al. 2018), which can be directly tested against observations via the concentration measurement (e.g., Oguri et al. 2012; Merten et al. 2015). An accurate account of the cluster mass distribution requires mass estimates that are sensitive at the cores and at the outskirts of the galaxy cluster. Crucial to all cluster-based cosmological studies are the sample size, selection function, and good understanding of the systematic uncertainties of the mass estimates coming from

observed astrophysical properties (e.g., [Evrard et al. 2002](#); [Khedekar & Majumdar 2013](#); [Huterer & Shafer 2018](#); [Bocquet et al. 2019](#)).

One of the methods to measure the total (dark and baryonic) mass distribution of galaxy clusters is using gravitational lensing. Weak lensing (WL) measures the cluster mass at large cluster-centric radii, while strong lensing (SL) has the highest resolution at the core of the cluster where the SL evidence is present. The combination of the core mass estimates from SL and outskirts mass estimates from WL or other large scale mass proxies can constrain the mass distribution profile of a galaxy cluster, and measure its concentration (e.g., [Gralla et al. 2011](#); [Oguri et al. 2012](#); [Merten et al. 2015](#); [Meneghetti et al. 2010](#)). Comparisons between the predicted and observed properties of SL galaxy clusters mass distribution have reported possible tension (e.g., [Broadhurst & Barkana 2008](#); [Gonzalez et al. 2012](#); [Meneghetti et al. 2013](#); [Killedar et al. 2018](#)), however these studies have been limited by complicated selection function and small sample sizes.

Current and upcoming large surveys will discover thousands of SL clusters out to  $z \sim 2$ , using methods that span the wavelength spectrum. Some of these surveys include the South Pole Telescope (SPT; [SPT-3G, Benson et al. 2014](#); [SPT-SZ 2500 deg<sup>2</sup>, Bleem et al. 2015](#)), Vera Rubin Observatory Legacy Survey of Space and Time (LSST, [LSST Science Collaboration et al. 2017](#)), and eROSITA ([Pillepich et al. 2018](#)). These large samples will require a method to timely, effectively, and accurately measure the core mass of SL clusters.

Strong-lensing based mass measurements are typically based on detailed strong lensing models (e.g., [Kneib & Natarajan 2011](#)). Detailed lens models for galaxy clusters with rich strong lensing evidence, such as the Frontier Fields clusters ([Lotz et al. 2017](#)) but also less extraordinary clusters, allow for the high degree of complexity required to study substructure in the mass distribution of the cluster (e.g., [Ebeling et al. 2017](#); [Mahler et al. 2018](#); [Richard et al. 2020](#)). They necessitate extensive follow-up observations, computational resources, and multiple statistical assessments for the best model selection. However, more typical SL clusters have a small number of SL constraints, which limits the utility of detailed lens models (e.g., [Smith et al. 2005](#); [Sharon et al. 2020](#)).

The large sample sizes of SL clusters being discovered calls for efficient methods to estimate the mass at the core of galaxy clusters. [Remolina González et al. \(2020\)](#) and [Remolina González et al. \(2021\)](#) evaluated two methods for efficiently estimating the mass within the core of SL clusters using the Outer Rim cosmological

simulation. [Remolina González et al. \(2020\)](#) evaluated the mass estimate derived from the size of the Einstein radius; [Remolina González et al. \(2021\)](#) assessed results from simplified single-halo lens models. The characterization of uncertainty and bias of these methods established them for the application to large samples of SL galaxy clusters as efficient and accurate galaxy cluster core mass estimators. The two simulation-calibrated methods take orders of magnitude less time and human intervention than detailed lens models.

The goal of this paper is to test, in real observed clusters, how well these first- and second-order estimates of the core mass compare to detailed lens models. This paper is organized as follows. In §2, we introduce the three strong lensing cluster samples used in our paper and describe our selection of the detailed lens models. In §3, we briefly describe the publicly available lensing algorithms used to compute the detailed lens models and summarize the single-halo lens model and Einstein radius methods used as efficient estimates of the mass at the core of galaxy clusters. In §4, we describe the strong lensing constraints and selection of the brightest cluster galaxy (BCG), and compute the empirically-corrected mass enclosed by the Einstein radius ( $M_{corr}(< \theta_E)$ ) and the aperture mass enclosed by the effective Einstein radius ( $M_{SHM}(< e\theta_E)$ ) from the single-halo lens models that passed a quick visual inspection. In §5, we measure the scatter and bias of  $M_{corr}(< \theta_E)$  and  $M_{SHM}(< e\theta_E)$  compared to the mass enclosed by the same aperture in the detailed lens model ( $M_{DLM}$ ) and explore any possible difference due to the variety of lensing algorithms utilized to compute the detailed lens models. Last in §6, we present our conclusions and summarize the application of efficient methods to measure the core masses of galaxy clusters.

In our analysis, we adopt a flat  $\Lambda$ CDM cosmology:  $\Omega_\Lambda = 0.7$ ,  $\Omega_M = 0.3$ , and  $H_0 = 70 \text{ km s}^{-1} \text{ Mpc}^{-1}$ , which was used by most of the detailed lens models included in our analysis. The GLAFIC detailed lens models of the RELICS clusters follow a Wilkinson Microwave Anisotropy Probe Cosmology ([Komatsu et al. 2011](#)):  $\Omega_\Lambda = 0.728$ ,  $\Omega_M = 0.727$ , and  $H_0 = 70.4 \text{ km s}^{-1} \text{ Mpc}^{-1}$ . The large scale masses are reported in terms of  $M_{\Delta c}$ , defined as the mass enclosed within a radius at which the average density is  $\Delta$  times the critical density of the universe at the cluster redshift.

## 2. OBSERVATIONAL DATA

For this work, we use the data from four well-established strong lensing surveys of clusters with different selections functions. First, the Sloan Giant Arcs

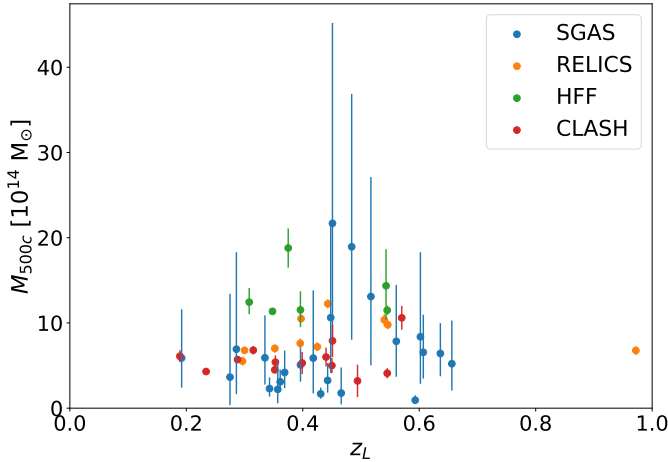


**Figure 1.** Redshift-Mass ( $z_L - M_{500c}$ ) distribution of the strong lensing galaxy clusters used in our analysis.

Survey (SGAS<sup>1</sup>; Hennawi et al. 2008; Sharon et al. 2020) which identified highly magnified lensed galaxies in the Sloan Digital Sky Survey (SDSS; Abazajian et al. 2009; Blanton et al. 2017). Second, the Cluster Lensing and Supernova Survey with *Hubble* (CLASH<sup>2</sup>; Postman et al. 2012), designed to study the dark matter distribution in galaxy clusters, perform supernova searches, and detect and characterize high-redshift lensed galaxy clusters. Third, the *Hubble* Frontier Fields Clusters (HFF<sup>3</sup>; Lotz et al. 2017) which are some of the best strong lensing clusters, taking advantage of deep imaging and extensive spectroscopic follow-up. Fourth, the Reionization Lensing Cluster Survey (RELICS<sup>4</sup>; Coe et al. 2019), designed primarily to find high-redshift ( $z \sim 6 - 8$ ) lensed galaxy candidates. All four samples base their lensing analyses on multiband *Hubble Space Telescope* (*HST*) imaging. From these samples of lensing galaxy clusters, we only include clusters with spectroscopically confirmed multiply imaged lensed galaxies. Figure 1 shows the redshift-mass distribution of the galaxy clusters used in our analysis. The large scale masses,  $M_{500c}$ , are taken from Fox et al. (in preparation), Merten et al. (2015), and references therein.

### 2.1. SGAS

Galaxy clusters were selected for the SGAS survey from the SDSS Data Release 7 (SDSS-DR7; Abazajian et al. 2009) using the cluster red-sequence algorithm by Gladders & Yee (2000). Color images were created from

imaging data in  $g$ ,  $r$ ,  $i$ , and  $z$  centered on the detected cluster. The images were visually inspected and scored according to the evidence of strong gravitational lensing. There has been extensive ground- and space-based imaging leading to a multi-wavelength picture of these clusters (e.g., 107 *HST* orbits of the SGAS-*HST*, GO13003 PI:Gladders; Sharon et al. 2020). Spectroscopic follow-up of all the primary strong lensing arcs is complete, and additional follow-up campaigns obtained redshifts of secondary arcs to improve the fidelity of the lens models (e.g., Bayliss et al. 2011b; Johnson et al. 2017; Sharon et al. 2020, and references therein). Several high-impact targets out of this sample of highly magnified arcs have been studied in detail (e.g., Koester et al. 2010; Bayliss et al. 2014; Sharon et al. 2017; Rigby et al. 2018).

The SGAS clusters are unique due to the selection function employed to create the sample, as they were selected uniquely based on the identification of bright strong lensing features. This led to including some clusters with lower masses when compared to the other three samples of galaxy clusters. Sharon et al. (2020) published and released to the community detailed lens models for the 37 SGAS clusters observed as part of *HST*-GO13003. Out of these 37 galaxy clusters with publicly available lens models (Sharon et al. 2020), we only use 31 in this work. Three clusters (SDSS J0004-0103, SDSS J1002+2031, and SDSS J1527+0652) are not included due to being poorly constrained (given a classification of C or lower; see Sharon et al. (2020) for more details). Two galaxy clusters (SDSS J1156+1911 and SDSS J1632+3500) lack any spectroscopically confirmed multiply imaged sources. One galaxy cluster (SDSS J2243-0935), has one spectroscopically confirmed flat giant arc, located between two cluster cores, making it unsuitable for the methods used here. In Table 1, the list of the SGAS clusters is shown with their corresponding redshift, the right ascension (R.A.) and declination (Decl.) of the selected BCG, and the number of strongly lensed background sources with spectroscopic redshifts that are used as lens modeling constraints.

### 2.2. CLASH

The Cluster Lensing and Supernova Survey with *Hubble* (CLASH; Postman et al. 2012) multi-cycle treasury project observed 25 galaxy clusters for a total of 525 *HST* orbits over a period of nearly three years utilizing 16 *HST* filters. The main science goals included: studying the matter distribution of galaxy clusters, particularly the mass concentration (e.g., Merten et al. 2015); detecting supernovae (e.g., Graur et al. 2014); and detecting and characterizing high-redshift galaxies magni-

<sup>1</sup> <https://archive.stsci.edu/pub/hlsp/sgas/>

<sup>2</sup> <https://www.stsci.edu/postman/CLASH/index.html>

<sup>3</sup> <https://outerspace.stsci.edu/display/HPR/HST+Frontier+Fields>

<sup>4</sup> <https://relics.stsci.edu/index.html>

fied by the galaxy cluster (e.g., [Coe et al. 2013](#)). From the 25 galaxy clusters, 20 are X-ray selected, dynamically relaxed (determined from their circularly symmetric X-ray surface brightness distribution), and massive clusters (X-ray temperatures  $T_x > 5$  keV). The majority of these clusters showed strong lensing evidence from ancillary data. The last five galaxy clusters were selected solely for being exceptional strong lenses. Four of the galaxy clusters (Abell S1063, MACS J0416.1–2403, MACS J0717.5+3745, and MACS J1149.5+2223) were later selected for the Hubble Frontier Fields (HFF; see §2.3) and we only utilize the HFF lens models for these clusters. The community follow-up effort has resulted in the identification of many lensing constraints with measured spectroscopic redshifts for the 13 galaxy clusters included in this work. Detailed lensing models by [Zitrin et al. \(2015\)](#) and [Caminha et al. \(2019\)](#) have been made publicly available. In [Table 1](#), we list the CLASH galaxy clusters utilized in our analysis and their corresponding references.

### 2.3. HFF

The *Hubble* Frontier Fields (HFF; [Lotz et al. 2017](#)) project observed six galaxy clusters and adjacent (“parallel”) fields using Director’s discretionary time, obtaining extremely deep multi-band imaging (140 *HST* orbits per cluster for a total of 840 *HST* orbits of Director’s Discretionary Time) with the primary goal of studying the magnified background universe. The clusters were selected for their observability from space- (*HST*, *Spitzer*, and *JWST*) and ground-based observatories, their lensing strength, and the availability of pre-existing ancillary data. These galaxy clusters have become some of the most studied galaxy clusters due to the community investment in extensive multi-wavelength imaging and spectroscopic follow-up, resulting in large numbers of strong lensing constraints identified and used in the detailed lens models ([Johnson et al. 2014](#); [Zitrin et al. 2014](#); [Diego et al. 2016](#); [Jauzac et al. 2016](#); [Limousin et al. 2016](#); [Caminha et al. 2017](#); [Karman et al. 2017](#); [Kawamata et al. 2018](#); [Mahler et al. 2018](#); [Strait et al. 2018](#); [Lagattuta et al. 2019](#); [Sebesta et al. 2019](#); [Vega-Ferrero et al. 2019](#); [Raney et al. 2020a](#); and references therein). The HFF program provides a unique opportunity to study the statistical and systematic uncertainties in the lensing outputs, due to the large number of diverse lensing algorithms that have computed detailed lens models of these clusters (e.g., [Meneghetti et al. 2017](#); [Priewe et al. 2017](#); [Remolina González et al. 2018](#);

[Raney et al. 2020b](#) compare different aspects of the HFF lens models using different algorithms). In this work, we include the fourth version of the public lens models, which is the most recent release. The clusters and references to the models are listed in [Table 1](#).

### 2.4. RELICS

The RELICS program selected 41 galaxy clusters for shallow multi-band observation with *HST* for the primary goal to deliver a large sample of high-redshift ( $z \sim 6 - 8$ ) galaxies ([Salmon et al. 2018, 2020](#); [Mainali et al. 2020](#); [Strait et al. 2020](#)). 21 clusters were selected from a subsample of the most massive Planck clusters (using the Sunyaev-Zeldovich effect, [Sunyaev & Zeldovich 1970](#), to estimate their mass; [Planck Collaboration et al. 2016](#)). The other 20 cluster were selected based on a prior identification as prominent strong lenses in available imaging data. The reasoning used for this selection is the expectation that the mass of the galaxy cluster relates to its potential to have a large lensing cross-section, leading to an increase in the chance to find high-redshift lensed sources.

The selection function employed for assembling the list of RELICS clusters explores the high-mass parameter space. In addition, the wider and shallower imaging observing strategy (total of 188 *HST* orbits, GO 14096; PI Coe) is a clear example of the challenges confronted by lensing surveys where only the primary and some of the secondary arcs are readily identifiable, leading to a limited number of constraints available for the lens modeling analysis ([Acebron et al. 2018, 2019, 2020](#); [Cerny et al. 2018](#); [Cibirka et al. 2018](#); [Paterno-Mahler et al. 2018](#); [Mahler et al. 2019](#) and references therein). From the 41 galaxy clusters observed, 34 have publicly available detailed lens models and only 12 have publicly available spectroscopically confirmed multiple imaged sources. Following [Fox et al.](#) (in preparation), we inspect the unpublished detailed lens models and include in our analysis only models whose predicted lensed images are within  $1''.5$  of the observed lensing evidence, and do not produce critical curves or masses that are not justified by the lensing constraints. In [Table 1](#), we present the list of the RELICS clusters used in our analysis with their corresponding lens redshift, R.A. and Decl. of the selected BCG, and the number of background source spectroscopic redshifts that were used to constrain  $M_{corr}(< \theta_E)$  and  $M_{SHM}(< e\theta_E)$  in this paper.

**Table 1.** Strong Lensing Galaxy Clusters

Galaxy Cluster	$z_L$	R.A. (J2000)	Decl. (J2000)	Detailed Lens Models	$N(z_S)$	Arcs/Model Reference
SGAS						
SDSS J0108+0624	0.548	17.17511	6.41210	L	1	a,b
SDSS J0146−0929	0.447	26.73336	−9.49792	L	2	a,c
SDSS J0150+2725	0.306	27.50355	27.42676	L	1	a
SDSS J0333−0651	0.573	53.26940	−6.85635	L	1	a
SDSS J0851+3331	0.369	132.91194	33.51837	L	3	a,d
SDSS J0915+3826	0.396	138.91280	38.44952	L	2	a,d,e
SDSS J0928+2031	0.192	142.01889	20.52919	L	2	a
SDSS J0952+3434	0.357	148.16761	34.57947	L	1	a,f
SDSS J0957+0509	0.448	149.41330	5.15885	L	1	a,d
SDSS J1038+4849	0.431	159.68159	48.82159	L	3	a,d
SDSS J1050+0017	0.593	162.66637	0.28522	L	3	a,g
SDSS J1055+5547	0.466	163.76917	55.80647	L	2	a,d
SDSS J1110+6459	0.656	167.57386	64.99664	L	1	a,c,h
SDSS J1115+1645	0.537	168.76845	16.76058	L	2	a,c,i
SDSS J1138+2754	0.451	174.53731	27.90854	L	2	a,d
SDSS J1152+0930	0.517	178.19748	9.50409	L	1	a
SDSS J1152+3313	0.361	178.00077	33.22827	L	2	a,d
SDSS J1207+5254	0.275	181.89965	52.91644	L	1	a,f
SDSS J1209+2640	0.561	182.34877	26.67950	L	2	a,d,j
SDSS J1329+2243	0.443	202.39391	22.72106	L	1	a,g
SDSS J1336−0331	0.176	204.00035	−3.52496	L	2	a
SDSS J1343+4155	0.418	205.88685	41.91763	L	1	a,d,k
SDSS J1420+3955	0.607	215.16680	39.91859	L	2	a,d
SDSS J1439+1208	0.427	219.79076	12.14043	L	2	a
SDSS J1456+5702	0.484	224.00368	57.03898	L	1	a
SDSS J1522+2535	0.602	230.71985	25.59097	L	1	a
SDSS J1531+3414	0.335	232.79429	34.24031	L	2	a,d
SDSS J1604+2244	0.286	241.04227	22.73858	L	1	a
SDSS J1621+0607	0.343	245.38494	6.12197	L	2	a,d
SDSS J1723+3411	0.442	260.90068	34.19948	L	2	a,f
SDSS J2111−0114	0.636	317.83062	−1.23984	L	1	a,d
CLASH						
Abell 383	0.189	42.01409	−3.52938	LTM.v2, NFW.v2	4	l,n,s,t,u
Abell 611	0.288	120.23673	36.05656	LTM.v2, NFW.v2	2	l,v
MACS J0329.7−0211	0.450	52.42321	−2.19623	L.v1, LTM.v2, NFW.v2	7	l,m,n
MACS J0416.1−2403	0.396	64.03808	−24.06750	See HFF	37	See HFF
MACS J0429.6−0253	0.399	67.40003	−2.88521	L.v1, LTM.v2, NFW.v2	2	l,m

*Table 1 continued*

**Table 1** (*continued*)

Galaxy Cluster	$z_L$	R.A. (J2000)	Decl. (J2000)	Detailed Lens Models	$N(z_S)$	Arcs/Model Reference
MACS J0717.5+3745	0.545	109.39855	37.75479	See HFF	8	See HFF
MACS J1115.9+0129	0.353	168.96628	1.49861	L.v1, LTM.v2, NFW.v2	2	l,m,n
MACS J1149.5+2223	0.543	177.39875	22.39853	See HFF	7	See HFF
MACS J1206.2−0847	0.440	181.55064	−8.80094	LTM.v2, NFW.v2	4	l,n,w,x
MACS J1311.0−0310	0.494	197.75751	−3.17770	L.v1, LTM.v2, NFW.v2	1	l,m
MACS J1423.8+2404	0.545	215.94949	24.07846	LTM.v2, NFW.v2	2	l,y
MACS J1931.8−2635	0.352	292.95684	−26.57587	L.v1, LTM.v2, NFW.v2	7	l,m
MACS J2129.7−0741	0.570	322.35879	−7.69105	L.v1, LTM.v2, NFW.v2	11	l,m,o
MS J2137−2353	0.315	325.06316	−23.66114	LTM.v2, NFW.v2	2	l
RXC J1347.5−1145	0.451	206.88261	−11.75318	L.v1, LTM.v2, NFW.v2	4	l,m,n,p,q,r
RXC J2129.7+0005	0.234	322.41649	0.08922	L.v1, LTM.v2, NFW.v2	7	l,m
RXC J2248.7−4431	0.348	342.18321	−44.53089	See HFF (Abell S1063)	18	See HFF (Abell S1063)
<b>HFF</b>						
Abell 2744	0.308	3.58626	−30.40017	C.v4, C.v4.1, D.v4 D.v4.1, G.v4, K.v4 S.v4c, W.v4	26	z,aa,ag,ah,ak,al,am
Abell 370	0.375	39.97133	−1.58224	B.v4, B.v4.1, C.v4 D.v4, D.v4.1, G.v4 K.v4, S.v4, W.v4 W.v4.1	32	z,ag,ai,aj,al,am
Abell S1063	0.348	342.18321	−44.53089	C.v4, C.v4.1, D.v4 D.v4.1, G.v4, K.v4 S.v4, W.v4, W.v4.1	18	z,ab,af,ag,al,am
MACS J0416.1−2403	0.396	64.03808	−24.06750	Cam.v4, C.v4, C.v4.1 D.v4, D.v4.1, G.v4 K.v4, S.v4c, W.v4	37	z,ae,ag,al,am
MACS J0717.5+3745	0.545	109.39855	37.75479	C.v4, C.v4.1, D.v4 D.v4.1, K.v4, S.v4c W.v4, W.v4.1	8	z,ad,al,am
MACS J1149.5+2223	0.543	177.39875	22.39853	C.v4, C.v4.1, D.v4 D.v4.1, K.v4, S.v4c W.v4	7	z,ac,al,am
<b>RELICS</b>						
Abell 2537	0.297	347.09256	−2.19212	L.v1, G.v2	1	an
Abell 3192	0.425	59.72531	−29.92527	L.v1	2	ao
Abell S295	0.300	41.35339	−53.02932	LTM.v2	1	ap
CL J0152.7−1357	0.833	28.18242	−13.95515	L.v1, LTM.v1, G.v2	1	aq
MACS J0025.4−1222	0.586	6.36415	−12.37303	LTM.v1	1	ap
MACS J0035.4−2015	0.352	8.85889	−20.26229	L.v1, G.v2	2	au

*Table 1 continued*



Table 1 (continued)

Galaxy Cluster	$z_L$	R.A. (J2000)	Decl. (J2000)	Detailed Lens Models	$N(z_S)$	Arcs/Model Reference
MACS J0417.5–1154	0.443	64.39454	–11.90885	L.v2, G.v3	2	ar
PLCK G004.5–19.5	0.540	289.27098	–33.52236	L.v1	5	au
RXC J0018.5+1626	0.546	4.63992	16.43787	L.v1	2	au
RXC J0032.1+1808	0.396	8.03914	18.11561	L.v1, LTM.v2, G.v2	1	as
RXC J2211.7–0350	0.397	332.94137	–3.82895	L.v1, G.v2	1	an
SPT–CL J0615–5746	0.972	93.96543	–57.78011	L.v1, LTM.v1	2	at

**Strong Lensing Galaxy Clusters Included in this Work.**  $z_L$  is the lens redshift of the galaxy cluster, R.A. and Decl. are the right ascension and declination of the selected BCG, respectively, and  $N(z_S)$  is the number of multiply-imaged lensed background sources with spectroscopic redshifts that are used in this paper. The Detailed Lens Models lists indicate the name of the lens modeling teams or algorithms, and the versions which are utilized for the comparison in this work. A brief description of the samples can be found in §2: SGAS (see §2.1), CLASH (see §2.2), HFF (see §2.3), and RELICS (see §2.4).

NOTE—

Detailed Lens Models used in this work (see also §2):

SGAS: L = **Lenstool**

CLASH: L = **Lenstool**; LTM = Light-Traces-Mass; NFW = LTM + eNFW; .v1 = version 1; .v2 = version 2

HFF: B = Bradač (SWUnited); C = CATS (**Lenstool**); Cam = Caminha (**Lenstool**); D = Diego (WSLAP+); G = Glafic (GLAFIC); K = Keeton (**GRAVLENS**); S = Sharon (**Lenstool**); W = Williams (GRALE); .v4 = version 4; .v4c = version 4 corrected; .v4.1 = version 4.1

RELICS: G = GLAFIC; L = **Lenstool**; LTM = Light-Traces-Mass; .v1 = version 1; .v2 = version 2; .v3 = version 3

References:

a) Sharon et al. (2020); b) Rigby et al. (2018); c) Stark et al. (2013); d) Bayliss et al. (2011a); e) Bayliss et al. (2010); f) Kubo et al. (2010); g) Bayliss et al. (2014); h) Johnson et al. (2017); i) Bayliss (2012); j) Ofek et al. (2008); k) Diehl et al. (2009); l) Zitrin et al. (2015); m) Caminha et al. (2019); n) CLASH-VLT Rosati et al. (in prep); o) Huang et al. (2016); p) Ravindranath & Ho (2002); q) Bradač et al. (2008); r) Halkola et al. (2008); s) Smith et al. (2001); t) Newman et al. (2011); u) Richard et al. (2011); v) Newman et al. (2013); w) Ebeling et al. (2009); x) Zitrin et al. (2012); y) Limousin et al. (2010); z) Johnson et al. (2014); aa) Zitrin et al. (2014); ab) Diego et al. (2016); ac) Jauzac et al. (2016); ad) Limousin et al. (2016); ae) Caminha et al. (2017); af) Karman et al. (2017); ag) Kawamata et al. (2018); ah) Mahler et al. (2018); ai) Strait et al. (2018); aj) Lagattuta et al. (2019); ak) Sebesta et al. (2019); al) Vega-Ferrero et al. (2019); am) Raney et al. (2020a); an) Cerny et al. (2018); ao) Hsu et al. (2013); ap) Cibirka et al. (2018); aq) Acebron et al. (2019); ar) Mahler et al. (2019); as) Acebron et al. (2020); at) Paterno-Mahler et al. (2018); au) RELICS public data release (see §2.4)

### 3. LENS MODELING AND EINSTEIN RADIUS

Strong lens modeling analyses use the positional and redshift measurements of lensed galaxies (arcs) as constraints to model the underlying mass distribution. There is a variety of well-established lensing algorithms that have been used extensively to study both the galaxy cluster and the magnified background universe. Below, we provide a brief description of the lensing algorithms that were employed to compute the publicly available detailed lens models used in our analysis. We also briefly describe the Einstein Radius mass estimate, and single-halo lens models, which were recently evaluated by Remolina González et al. (2020) and Remolina González et al. (2021), respectively, as methods to quickly and effectively measure the mass at the core of strong lensing galaxy clusters.

#### 3.1. Detailed Lens Models

Lensing algorithms are usually grouped into three categories: parametric, non-parametric, and hybrid, based on the parametrization of the modeled mass distribution. Parametric models utilize a combination of parametric functions to describe the mass distribution of the lens plane. Non-parametric or “free-form” algorithms make no assumption on the functional form of the mass distribution. Hybrid models are a combination of these two forms. The degree to which mass is assumed to be correlated with the observed light distribution also varies among the different algorithms.

The parametric models that are used in this work include: GLAFIC (Oguri 2010; Ishigaki et al. 2015; Kawamata et al. 2016), **GRAVLENS** (Keeton 2011; McCully et al. 2014), and **Lenstool** (Jullo et al. 2007; Jullo & Kneib 2009; Niemiec et al. 2020). These algorithms use a variety of analytical mass distributions

both for the cluster-scale dark matter halos and the contribution of the galaxy cluster members. Light-Traces-Mass (LTM; Broadhurst et al. 2005; Zitrin et al. 2009, 2015) assigns mass to a parameterized description of the light distribution, and LTM with elliptical NFW profiles (LTM+eNFW; Zitrin et al. 2009, 2015) combines this approach with analytical mass distributions as the parametric models. The “free-form” algorithms include Strong and Weak Lensing United (SWUnited; Bradač et al. 2006, 2009) which performs an iterative minimization of a non-regular adaptive grid and GRALE (Liesenborgs et al. 2006; Mohammed et al. 2014), which uses a genetic algorithm to iteratively refine the mass distribution on a grid. Last, the hybrid algorithm Weak & Strong Lensing Analysis Package (WSLAP+; Diego et al. 2007, 2016) is a non-parametric algorithm with the addition of a parametrized distribution for the cluster member contribution. Modeling algorithms also differ by their assumptions on the extent of correlation between light and mass. A variety of techniques are employed to explore the parameter space and determine the model that best reproduces the observed lensing configuration, and determine statistical uncertainties.

Detailed lens models (DLM) can be highly complex, adding the flexibility required for detailed studies of galaxy cluster properties, their surrounding environment, uncorrelated structure along the line-of-sight, the magnified background universe, and cosmology. This high complexity of the models relies on a large number of free parameters, requiring a large number of constraints, i.e., multiply-imaged lensed galaxies, whose availability becomes a limiting factor in the modeling process. The versatility of DLM also means the models are not unique and require care in the construction and evaluation; statistical assessments are employed to select between models (e.g., Acebron et al. 2017; Paterno-Mahler et al. 2018; Lagattuta et al. 2019; Mahler et al. 2019). High-fidelity lens models of galaxy clusters with rich strong lensing evidence require extensive follow-up observations, large investment of computational and human resources, and multiple iterations of the lensing analysis and modeling process to revise the models as new observational evidence becomes available (e.g., Sharon et al. 2012; Johnson et al. 2014; Jauzac et al. 2015).

To determine the statistical uncertainties of the public DLM used in this work, we use the “range” maps that are provided with them. The “range” maps are the same lensing products as the best-fit products, except they are derived from sets of parameters that sample the parameter space of each model, and provide a handle on how the variation in model parameters affects the lensing-derived projected mass density.

### 3.2. Single-Halo Lens Models

The single-halo lens models (SHM) computed in this analysis follows Remolina González et al. (2021). We use `Lenstool` to compute the SHM in one lens plane with a single cluster-scale dark matter halo. The mass distribution is parameterized using a dual pseudo-isothermal ellipsoid (dPIE, Elíasdóttir et al. 2007) and no contribution from galaxy cluster members. Of the seven dPIE parameters ( $\Delta\alpha$  and  $\Delta\delta$  are the R.A. and Decl.;  $\epsilon$  is the ellipticity;  $\theta$  is the position angle;  $r_{core}$  is the core radius;  $r_{cut}$  is the truncation radius; and  $\sigma$  is the effective velocity dispersion), only six are optimized as we set the truncating radius to a fixed 1500 kpc as is typically done in DLM in the literature (note that this projected radius is also similar to the splashback radius; e.g., Umetsu & Diemer 2017; Shin et al. 2019). We use broad priors in the six free parameters of the dPIE potential:  $-8''.0 < \Delta\alpha, \Delta\delta < 8''.0$ ;  $0.0 < \epsilon < 0.9$ ;  $0^\circ < \theta < 180^\circ$ ;  $50 \text{ kpc} < r_{core} < 150 \text{ kpc}$ ; and  $500 \text{ km/s} < \sigma < 1500 \text{ km/s}$ . The small number of free parameters calls for only a handful of constraints, with a minimum of 6 constraints required. This can be satisfied with as little as 4 multiple images of the same source, as each identified set of  $n$  multiple images contributes  $2n - 2$  constraints. With the image identification in hand (see §4.1), the models can be computed quickly and with limited human intervention. Generally, the SHM can be automatically computed once the cluster redshift, center initial position (e.g., the brightest cluster galaxy - BCG), and position and redshift of the arcs are measured.

Remolina González et al. (2021) used the lensing products from the SHM best fit model to compute the effective Einstein radius,  $e\theta_E$ , and measure mass enclosed by this aperture,  $M_{SHM}(< e\theta_E)$ . The effective Einstein radius is defined as the radius of a circle with the same area as the area enclosed by the tangential critical curve. Remolina González et al. (2021) found an overall scatter of 8.5% with a bias of 0.9% in  $M_{SHM}(< e\theta_E)$ . When a quick visual inspection is performed and only the models that pass the inspection are used, the scatter and bias of  $M_{SHM}(< e\theta_E)$  improve to 3.3% and 0.3%, respectively. The visual inspection is conducted to identify those single-halo lens models that fail to reproduce the observed lensing configuration and predict arcs in regions where no multiple images are found.

### 3.3. Einstein Radius

The mass enclosed by the Einstein radius,  $M(< \theta_E)$ , is a quick method to estimate cluster core mass, where strong lensing is detected:

$$M(< \theta_E) = \Sigma_{cr}(z_L, z_S) \pi [D_L(z_L)\theta_E]^2, \quad (1)$$



where  $\Sigma_{cr}(z_L, z_S)$  is the critical surface density,  $D_L(z_L)$  is the angular diameter distance from the observer to the lens,  $z_L$  is the lens redshift,  $z_S$  is the background source redshift, and  $\theta_E$  is the Einstein radius, which can be measured from the occurrence of arcs around the center of the lens. The main assumption of this method is that the projected mass distribution of the lens is circularly symmetric (Narayan & Bartelmann 1996; Schneider 2006; Kochanek 2006; Bartelmann 2010; Kneib & Natarajan 2011).

Remolina González et al. (2020) quantified the scatter and bias of the mass enclosed by the Einstein radius and introduced empirical corrections based on simulations. The method was calibrated for Einstein radii  $\leq 30''$ , for different centering assumptions. The corrected mass enclosed by the Einstein radius,  $M_{corr}(< \theta_E)$ , is reported to have no bias, and a scatter of 10.9% for the quadratic (12.1% for the linear) corrected masses. Only the identified tangential arcs are used in this method.

Following the recommendation and procedures established by Remolina González et al. (2020), when applying this method to the observational data we use the BCG of the galaxy cluster as our fixed center.

The projected arc radii in this work extend beyond the calibrated range (see Figure 2). We therefore use caution when applying this method to our sample, and investigate different choices in its application at large Einstein radii. We apply the quadratic empirical correction for Einstein radii  $\leq 30''$ , as recommended by Remolina González et al. (2020), and the linear empirical correction for the rest. In addition to the full sample, we report results for a subsample of  $\leq 20''$ , which is better represented by the simulated data used by Remolina González et al. (2020) to calibrate the method.

#### 4. METHODOLOGY

In the following section, we describe the input constraints needed to compute  $M(< \theta_E)$  and  $M_{SHM}(< e\theta_E)$ . Following the work by Remolina González et al. (2020) and Remolina González et al. (2021), we compute the core mass for the sample of strong lensing galaxy clusters analysed in this work.

##### 4.1. Arc Catalogs

We use the lensing constraints (arcs) that were identified and listed with the public lens models. For this work, we only use constraints with spectroscopic redshifts (reference for the arc catalogs are given in §2). We inspect the lensed galaxies and determine if they are tangential or radial arcs depending on the direction of their distortion. Only the tangential arcs are used for fitting the Einstein radius, but all of the arcs are included when computing the single-halo lens models.

##### 4.2. BCG Selection

The position of the BCG serves as the initial position for the cluster-scale dark matter halo in the single-halo lens models and as the fixed center in the Einstein radius mass estimate. The BCGs were selected by their magnitude from a cluster member catalog (see Postman et al. 2012 and Fox et al. (in preparation)) and then confirmed by visual inspection.

##### 4.3. Computing $M_{SHM}(< e\theta_E)$ and $M_{corr}(< \theta_E)$

Using the catalog of the arcs and the selected BCG, we compute the single-halo lens models and measure the Einstein radii of the observed clusters. We compute a SHM for each set (also known as “family”) of multiply-imaged background sources. There are cases where a galaxy cluster has multiple arc families although none of the individual families satisfy the minimum number of 6 constraints needed. We therefore compute one SHM for each cluster that uses all the families as constraints, thus the minimum number of constraints needed is attained (the total number of constraints for a given model is  $\Sigma(2n_i - 2)$ , where  $n_i$  is the number of constraints for background source  $i$ ). All the SHM are inspected and only the ones that pass the quick visual inspection are used in our analysis. From the total of 62 clusters, 59 (29 SGAS, 12 RELICS, 6 HFF, and 12 CLASH) have enough constraints to compute a SHM, i.e., 6 or more constraints. Following the visual inspection, only 52 (23 SGAS, 11 RELICS, 6 HFF, and 12 CLASH) clusters remain in our analysis.

We plot the distribution of effective Einstein radii measured from the single-halo lens models that pass the visual inspection in Figure 2. The distribution of  $e\theta_E$  from the SHM generally follows the number of clusters in each survey, as most clusters only have one or two independent SHM that could be computed and pass the visual inspection. We note that while the depth of the HFF data leads to an unprecedented number of strongly lensed galaxies overall, many of the arc families do not have four or more secure multiple images each. We find that SGAS models occupy the lower end of the effective Einstein radius distribution, followed by RELICS, CLASH, and HFF. The distributions of  $e\theta_E$  emphasizes the difference in the selection function of the strong lensing sample, as CLASH, HFF, and RELICS attempted to select clusters with large lensing cross section, to increase the chances of observing magnified high redshift galaxies. The resulting SHM outputs are used to compute  $M_{SHM}(< e\theta_E)$  as described in §3.2.

Utilizing the same catalog of arcs and BCG positions, we geometrically fit this data with a circle, following Remolina González et al. (2020). We measure at least one

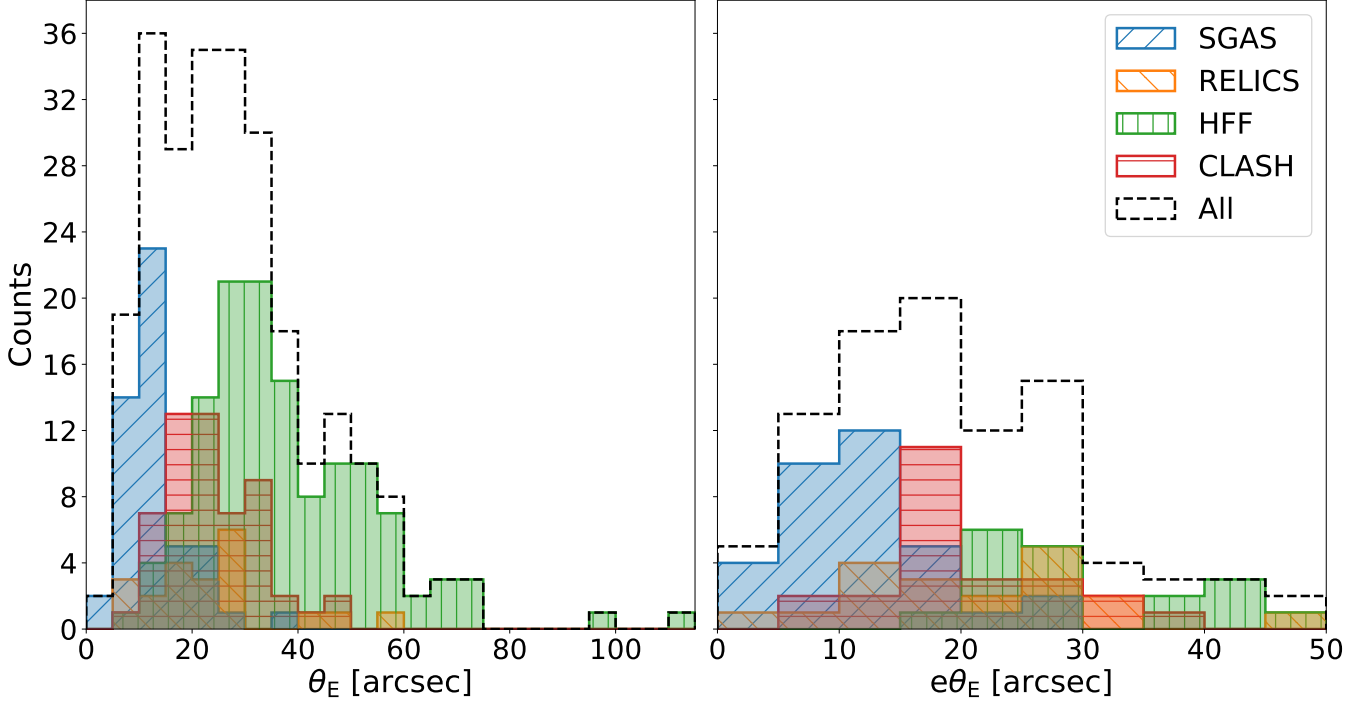


**Figure 2. Distribution of  $\theta_E$  and  $e\theta_E$  as measured from the two different mass estimate methods.** The Einstein radius ( $\theta_E$ ; *Left panel*) is measured from the geometric fit of a circle to the identified tangential arcs of a single background source and the effective Einstein radius ( $e\theta_E$ ; *Right panel*) is measured as the radius of a circle with the same area enclosed by the tangential critical curve of the single-halo lens models that passed the visual inspection. Both  $\theta_E$  and  $e\theta_E$  have units of arcseconds. The black dashed line represents the total counts and the colors denote the counts from the four different surveys of strong lensing galaxy clusters. As expected from the selection functions of these samples, SGAS clusters have lower  $\theta_E$  and  $e\theta_E$ , followed by the RELICS, CLASH, and HFF galaxy clusters. The deep observation and extensive followup of the six HFF clusters result in a large number of lensed sources with spectroscopic redshifts, extending to large cluster-centric radii, which is reflected in the distribution of  $\theta_E$ . SGAS, CLASH (except for those that are also part of HFF), and RELICS have only a few lensed sources per cluster with spectroscopic redshifts, and are found at smaller cluster-centric distances.

Einstein radius per galaxy cluster. We plot the distribution of all  $\theta_E$  in Figure 2. Unlike the SHM case, the  $M_{corr}(< \theta_E)$  can be computed for any number of multiple images of a given lensed source, resulting in a  $\theta_E$  measurement for each strongly-lensed source with spectroscopic redshift. The deep observations and extensive spectroscopic followup of the 6 HFF clusters resulted in a large number of lensed sources with spectroscopic redshifts, which extend to large cluster-centric radii. In all the other fields, where only a few lensed sources per cluster have spectroscopic redshifts, the number of measurements is driven by the number of clusters in each sample, and the identified sources have smaller cluster-centric distances. The Einstein radius is then used to compute  $M_{corr}(< \theta_E)$  as described in §3.3.

#### 4.4. Statistics

Depending on the number of arcs and arc families available for each method, each cluster enables up to 37  $\theta_E$  measurements and up to six SHM measurements. The measurements in each cluster are expected to be

correlated, and their distribution can inform the statistical uncertainty. On the other hand, individual clusters are independent of each other.

To validate the robustness of our rapid measurements, we follow Remolina González et al. (2020, 2021) and build a statistical sample for each method ( $\theta_E$  and SHM) to take into account multiple mass estimates for a single galaxy cluster and set the statistical weight for each cluster equal to one. For each galaxy cluster, we select at random an Einstein radius and a effective Einstein radius from the measured Einstein radii and available single halo lens models that passed visual inspection. For comparison to  $M_{DLM}$ , if a cluster has more than one detailed lens model (see §2), one DLM was selected at random. Then, we sample the selected mass measurement from a normal distribution centered at the best fit and standard deviation equal to the uncertainty. This process is repeated 1,000 times per cluster leading to a sample of 62,000  $M_{corr}(< \theta_E)$  points, 59,000 points from all SHM, of which 52,000  $M_{SHM}(< e\theta_E)$  points are ones that passed the quick visual inspection.

## 5. ANALYSIS OF RESULTS

In the following section, we compare the galaxy cluster core mass measurement between the Einstein radius,  $M_{corr}(< \theta_E)$ , and the single halo lens models,  $M_{SHM}(< e\theta_E)$ , to the mass enclosed by the respective mass apertures from the detailed lens models. We discuss the difference in the uncertainty measured in this work and the scatter measured from simulations by [Remolina González et al. \(2020, 2021\)](#). Last, we compare the scatter of two efficient mass methods,  $M_{corr}(< \theta_E)$  and  $M_{SHM}(< e\theta_E)$ , to the statistical modeling uncertainty of the detailed lens models. In this work the scatter is defined as half of the difference between the 84th and 16th percentiles. The bias is determined from the median of the distribution.

### 5.1. Mass Enclosed by the Einstein Radius, $M_{corr}(< \theta_E)$

In [Figure 3](#), we plot the direct comparison between the corrected mass enclosed by the Einstein radius,  $M_{corr}(< \theta_E)$ , and the mass enclosed by the same aperture from the best-fit detailed lens model,  $M_{DLM}$ , for all clusters. We measure an overall scatter of 18.3% and bias of  $-7.5\%$  in  $M_{corr}(< \theta_E)$  compared to  $M_{DLM}$ . We find that the distribution is biased low, particularly at large  $M_{DLM}$  values. The observed negative bias is reduced from systems with large Einstein radius ( $\theta_E > 20''.0$ ). For Einstein radius  $< 20''.0$  the scatter is 14.4% and bias of  $-4.4\%$ . This bias could be possibly addressed by extending the work of [Remolina González et al. \(2020\)](#) to larger radii, by using simulations that include lower magnification lensed sources at larger cluster-centric distances.

### 5.2. Mass Estimate from Single Halo Lens Models, $M_{SHM}(< e\theta_E)$

We assess the results of the entire SHM sample, and the results of the subsample of models that passed the visual inspection. In [Figure 4](#), we plot the direct comparison between the aperture mass enclosed by the effective Einstein radius of the SHM that passed the visual inspection,  $M_{SHM}(< e\theta_E)$ , and the mass enclosed by the same aperture in the best-fit DLM,  $M_{DLM}$ . We measure an overall scatter of 8.4% and a bias of 0.4% between  $M_{SHM}(< e\theta_E)$  and  $M_{DLM}$  for the SHM that passed the quick visual inspection. For the entire SHM sample, we measure an overall scatter of 12.4% and a bias of 2.3% between the two masses. We find that the visual inspection helps decrease the scatter and bias between  $M_{SHM}(< e\theta_E)$  and  $M_{DLM}$ .

### 5.3. Comparison to the Statistical Uncertainty of the Detailed Lens Models

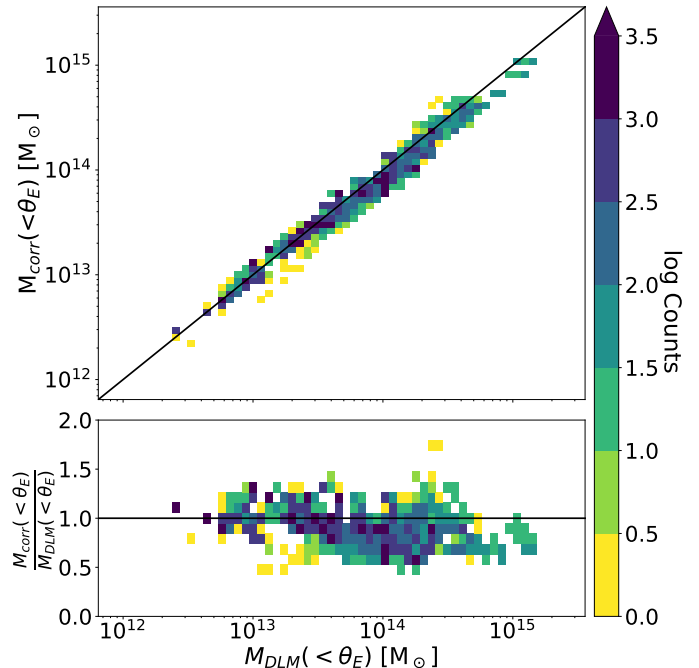


**Figure 3. Mass Comparison Between  $M_{corr}(< \theta_E)$  and  $M_{DLM}$ .** The *top* plot shows the direct mass comparison between the masses and the *bottom* plot is the mass ratio of the measurements. The total number of counts is the 62,000 sampled data points (see §4.4). The black lines indicate the one-to-one line, where  $M_{corr}(< \theta_E)$  equals  $M_{DLM}$ . We find that the distribution is biased low particularly at large  $M_{DLM}$ .

To contextualize the scatter of the mass estimates assessed in this paper, we review it against the uncertainty typically attributed to detailed lens models. We plot the overall scatter in the  $M_{corr}(< \theta_E)$  and  $M_{SHM}(< e\theta_E)$  measurements against the statistical uncertainty of the detailed lens models,  $\sigma(M_{DLM})$ , normalized by the best-fit DLM in [Figure 5](#). The statistical uncertainty of the detailed lens models is computed in the same way as the scatter (see §5), except the uncertainty of each data point is drawn from the publicly available “range” maps provided by the lensing teams, and represents a statistical sampling of the parameter space, typically using MCMC. The aggregated statistical uncertainty over the entire sample from the detailed lens models is  $\sigma(M_{DLM}) = 1.1\%$ .

However, the statistical DLM modeling uncertainty is likely underestimated. Comparing models of two simulated clusters that were computed by different DLM algorithms, [Meneghetti et al. \(2017\)](#) conclude that detailed lens models are reliable when recovering the enclosed mass in the inner  $100''.0$  with a scatter of less than 10%. In a recent comparison between DLM algorithms, [Raney et al. \(2020b\)](#) show that while the mass

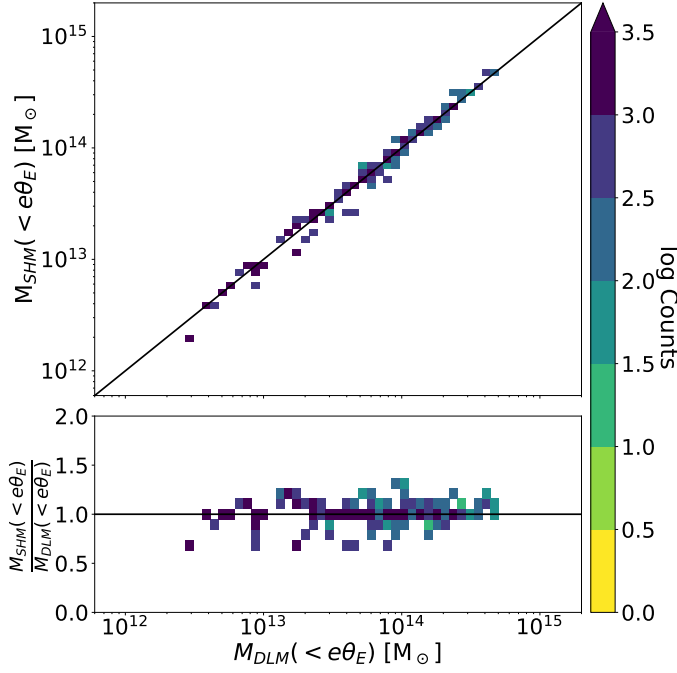


**Figure 4. Mass Comparison Between  $M_{\text{SHM}}(< e\theta_E)$  and  $M_{\text{DLM}}$ .** The *top* plot shows the direct mass comparison and the *bottom* plot shows the mass ratio. The total number of counts is the 52,000 sampled data points (see §4.4). The black lines indicate the one-to-one line, where  $M_{\text{SHM}}(< e\theta_E)$  equals  $M_{\text{DLM}}$ . We find that  $M_{\text{SHM}}(< e\theta_E)$  is unbiased compared to  $M_{\text{DLM}}$ .

measured by the detailed lens models is reliable, the statistical uncertainty reported by the lensing algorithms underestimates the systematic uncertainty. [Raney et al. \(2020b\)](#) estimate the systematic uncertainty at  $\sim 5\%$  for a circularly-averaged mass computed from the most recent versions (v4) of the HFF lens models.

#### 5.4. Comparison between Observations and Simulations

[Remolina González et al. \(2020, 2021\)](#) measured the scatter and bias of  $M_{\text{corr}}(< \theta_E)$  and  $M_{\text{SHM}}(< e\theta_E)$  against the “true” mass, from simulations. To compare the scatter found in this work to [Remolina González et al. \(2020, 2021\)](#), we need to account for the fact that detailed lens models are an observable measurement and while reliable are not the absolute truth. The expected scatter should therefore be a combination of the intrinsic scatter of the mass estimate, as measured from simulations, and the scatter attributed to the DLM measurement.

We note that the scatter between the three mass estimates ( $M_{\text{corr}}(< \theta_E)$ ,  $M_{\text{SHM}}(< e\theta_E)$ , and  $M_{\text{DLM}}$ ) may be correlated. To fully characterize the correlations between the masses will require the computation of de-

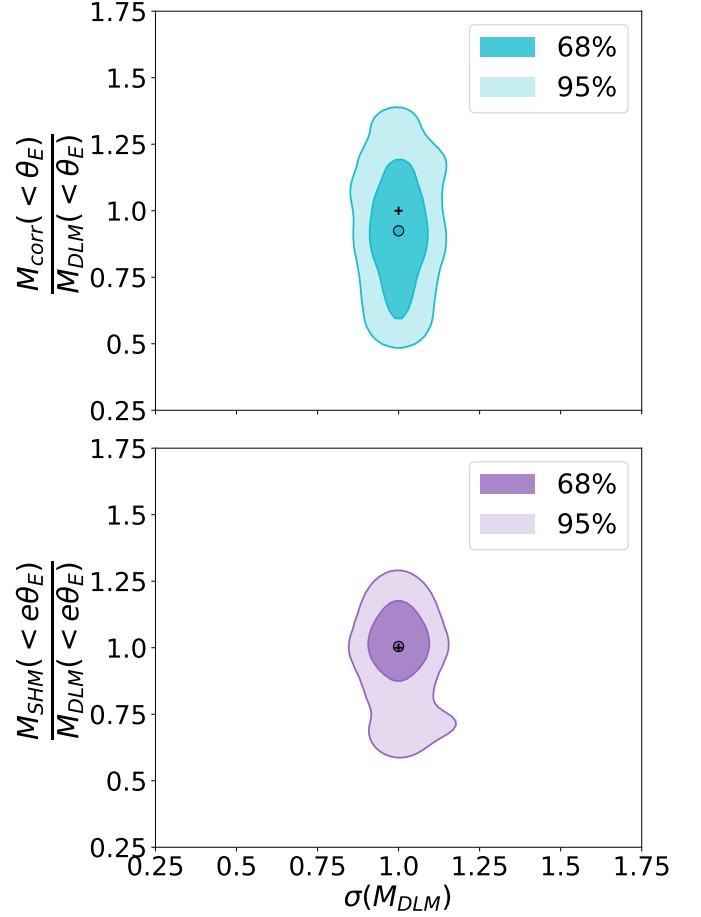


**Figure 5. The Scatter of the Efficient Mass Estimate Methods, Compared to the Statistical Uncertainty of the Detailed Lens Models.** We plot the mass ratio between the mass estimate and the best-fit detailed lens model against the statistical scatter of the detailed lens models,  $\sigma(M_{\text{DLM}})$ , derived from the publicly available “range” maps and normalized by the best-fit detailed lens model. The crosses stand for the point (1.0,1.0) and the open circles indicate the median of the distributions. Results for  $M_{\text{corr}}(< \theta_E)$  are shown in the *top* panel, and for  $M_{\text{SHM}}(< e\theta_E)$  in the *bottom* panel, smoothed by a kernel of 5%. The black cross indicates the location where  $M_{\text{corr}}(< \theta_E)$  and  $M_{\text{SHM}}(< e\theta_E)$  equal  $M_{\text{DLM}}$ .

tailed lens models for a large sample of simulated strong lensing galaxy clusters, which awaits new large cosmological simulations with baryonic information and will require an extensive amount of physical and human resources.

With this in mind, we compute a lower limit in the expected scatter by assuming that the scatter between the masses is un-correlated. We add in quadrature the scatter of  $M_{\text{corr}}(< \theta_E)$  and  $M_{\text{SHM}}(< e\theta_E)$  from simulations (10.9% and 3.3%, respectively, from [Remolina González et al. 2020, 2021](#)) with a 5% scatter in  $M_{\text{DLM}}$  (from

Raney et al. 2020b). This results in a expected scatter of 12.0% for  $M_{corr}(< \theta_E)$  and 6.0% for  $M_{SHM}(< e\theta_E)$  that passed the visual inspection. In both cases, we find that the overall scatter measured in this work (18.3% and 8.4%) is larger than expected. The difference between these scatters highlights some of the limitations in the simulation used by Remolina González et al. (2020, 2021) to account for the full range of scatter due to, e.g., baryonic effects, uncorrelated mass along the line of sight, and shear from nearby structures.

## 6. SUMMARY AND CONCLUSIONS

A large number of strong lensing galaxy clusters is expected to be detected in current and upcoming large surveys. Estimating the mass at the core of these galaxy clusters will serve as one of the anchors to the radial mass distribution profile and measurement of the concentration. Detailed lens models to analyze these strong lensing clusters and measure the mass at the core of the galaxy cluster are limited by the small number of constraints available from the identified multiply imaged lensed sources and can take multiple weeks to be finalized. Timely, efficient, and accurate methods to measure the mass at the core of galaxy clusters in these large samples are needed. Remolina González et al. (2020) assessed an empirically corrected mass enclosed by the Einstein radius ( $M_{corr}(< \theta_E)$ ) and Remolina González et al. (2021) assessed the aperture mass enclosed by the effective Einstein radius from the single-halo lens models ( $M_{SHM}(< e\theta_E)$ ) using simulated strong lensing images from the Outer Rim (Heitmann et al. 2019). In this work, we applied the two methods to observational data and used the publicly available detailed lens models from the SGAS, CLASH, HFF, and RELICS strong lensing cluster samples to evaluate the efficacy of the methods in measuring the core mass of galaxy cluster. We conclude the following:

- The corrected mass enclosed by the Einstein radius,  $M_{corr}(< \theta_E)$ , has an overall scatter of 18.3% and bias of  $-7.5\%$  compared to the detailed lens models. The bias is reduced if large ( $\theta_E > 20''$ ) Einstein radii are excluded. For Einstein radii  $< 20''$  the scatter is 14.4% and the bias is  $-4.4\%$ .
- The SHM aperture mass enclosed by the effective Einstein radius,  $M_{SHM}(< e\theta_E)$ , when computed over the entire sample, has an overall scatter of 12.4% and bias of 2.3% compared to the DLM. A quick visual inspection of the SHM outputs eliminates the SHM that fail to reproduce the lensing configuration, reducing the scatter to 8.4% and the bias to 0.4%. We find that the quick visual inspection

is beneficial in reducing the scatter and bias between  $M_{SHM}(< e\theta_E)$  and  $M_{DLM}$ , and identify lines of sight that would benefit from a more detailed analysis.

- To compare the overall scatter from  $M_{corr}(< \theta_E)$  and  $M_{SHM}(< e\theta_E)$  to that of simulations, we need to take into account the uncertainty in the detailed lens models. While we expect correlations between all mass estimates ( $M_{corr}(< \theta_E)$ ,  $M_{SHM}(< e\theta_E)$ , and  $M_{DLM}$ ), computing this is out of the scope of this analysis. We choose to compute a lower limit for the expected scatter by adding in quadrature 5%, which corresponds to the scatter of the mass from the detailed lens models, to the scatter measured in the simulation of 10.9% (3.3%) for  $M_{corr}(< \theta_E)$  ( $M_{SHM}(< e\theta_E)$  that passed the visual inspection). The resulting expected scatter is 12.0% for the corrected mass enclosed by the Einstein radius and 6.0% for the SMH that passed the visual inspection. The measured scatter in this work for both cases, 18.3% in  $M_{corr}(< \theta_E)$  and 8.4% in  $M_{SHM}(< e\theta_E)$ , is higher than our estimated lower limit of the expected scatter. The difference is then associated with limitations in the simulation used by Remolina González et al. (2020, 2021) including baryonic effects, line-of-sight structure, and shear due to nearby structures.
- Detailed lens models are considered to be the state of the art in measuring the enclosed projected mass density within the cores of galaxy clusters. While likely underestimated, the relative *statistical* lens modeling uncertainty of detailed lens models, marginalized over the large sample we investigated here, is of order 1.1%. Systematic uncertainties are estimated in the literature (e.g., Meneghetti et al. 2017; Raney et al. 2020b) at the 5 – 10% level. We show that the precision toll of using the significantly-faster mass estimate methods is only a 8.4% or 18.3% increase over the detailed lens models. We conclude that if other, larger, sources of error dominate the analysis, these fast and efficient mass estimate methods become a powerful tool in analyses of large cluster samples.

Overall, this work demonstrates the successful application of these efficient methods to observational data as currently established, as well as their reliability to estimate the mass at the core of strong gravitational lensing galaxy clusters. We look forward to improvements



to these methods benefiting from identification of strong lensing evidence by convolutional neural networks (e.g., Canameras et al. 2020; Huang et al. 2021; Morgan et al. 2021) and other machine learning algorithms to model the mass distribution of the SL clusters (e.g., Bom et al. 2019; Pearson et al. 2019).

## ACKNOWLEDGEMENTS

We thank the HFF, RELICS, CLASH, and SGAS projects for making their lens models publicly available. Some of the High Level Science Products (HLSP) presented in this paper were obtained from the Mikulski

Archive for Space Telescopes (MAST). STScI is operated by the Association of Universities for Research in Astronomy, Inc., under NASA contract NAS5-26555. JDRG acknowledges support by the National Science Foundation Graduate Research Fellowship Program under Grant No. DGE 1256260. GM received funding from the European Union’s Horizon 2020 research and innovation programme under the Marie Skłodowska-Curie grant agreement No MARACAS - DLV-896778. Argonne National Laboratory’s work was supported by the U.S. Department of Energy, Office of Science, Office of High Energy Physics, under contract DE-AC02-06CH11357.

## REFERENCES

- Abazajian, K. N., Adelman-McCarthy, J. K., Agüeros, M. A., et al. 2009, *ApJS*, **182**, 543
- Acebron, A., Jullo, E., Limousin, M., et al. 2017, *MNRAS*, **470**, 1809
- Acebron, A., Cibirka, N., Zitrin, A., et al. 2018, *ApJ*, **858**, 42
- Acebron, A., Alon, M., Zitrin, A., et al. 2019, *ApJ*, **874**, 132
- Acebron, A., Zitrin, A., Coe, D., et al. 2020, *ApJ*, **898**, 6
- Allen, S. W., Evrard, A. E., & Mantz, A. B. 2011, *Annual Review of Astronomy and Astrophysics*, **49**, 409
- Bartelmann, M. 2010, *Classical and Quantum Gravity*, **27**, 233001
- Bayliss, M. B. 2012, *ApJ*, **744**, 156
- Bayliss, M. B., Gladders, M. D., Oguri, M., et al. 2011a, *ApJ*, **727**, L26
- Bayliss, M. B., Hennawi, J. F., Gladders, M. D., et al. 2011b, *ApJS*, **193**, 8
- Bayliss, M. B., Johnson, T., Gladders, M. D., Sharon, K., & Oguri, M. 2014, *ApJ*, **783**, 41
- Bayliss, M. B., Wuyts, E., Sharon, K., et al. 2010, *ApJ*, **720**, 1559
- Benson, B. A., Ade, P. A. R., Ahmed, Z., et al. 2014, in *Millimeter, Submillimeter, and Far-Infrared Detectors and Instrumentation for Astronomy VII*, Vol. 9153, 91531P
- Blanton, M. R., Bershadsky, M. A., Abolfathi, B., et al. 2017, *AJ*, **154**, 28
- Bleem, L. E., Stalder, B., de Haan, T., et al. 2015, *The Astrophysical Journal Supplement Series*, **216**, 27
- Bocquet, S., Heitmann, K., Habib, S., et al. 2020, *ApJ*, **901**, 5
- Bocquet, S., Dietrich, J. P., Schrabback, T., et al. 2019, *ApJ*, **878**, 55
- Bom, C., Poh, J., Nord, B., Blanco-Valentin, M., & Dias, L. 2019, arXiv e-prints, arXiv:1911.06341
- Bradač, M., Clowe, D., Gonzalez, A. H., et al. 2006, *ApJ*, **652**, 937
- Bradač, M., Schrabback, T., Erben, T., et al. 2008, *ApJ*, **681**, 187
- Bradač, M., Treu, T., Applegate, D., et al. 2009, *ApJ*, **706**, 1201
- Broadhurst, T., Benítez, N., Coe, D., et al. 2005, *ApJ*, **621**, 53
- Broadhurst, T. J., & Barkana, R. 2008, *MNRAS*, **390**, 1647
- Caminha, G. B., Grillo, C., Rosati, P., et al. 2017, *A&A*, **600**, A90
- Caminha, G. B., Rosati, P., Grillo, C., et al. 2019, *A&A*, **632**, A36
- Canameras, R., Schuldt, S., Suyu, S. H., et al. 2020, arXiv e-prints, arXiv:2004.13048
- Cerny, C., Sharon, K., Andrade-Santos, F., et al. 2018, *ApJ*, **859**, 159
- Child, H. L., Habib, S., Heitmann, K., et al. 2018, *ApJ*, **859**, 55
- Cibirka, N., Acebron, A., Zitrin, A., et al. 2018, *ApJ*, **863**, 145
- Coe, D., Zitrin, A., Carrasco, M., et al. 2013, *ApJ*, **762**, 32
- Coe, D., Salmon, B., Bradač, M., et al. 2019, *ApJ*, **884**, 85
- Diego, J. M., Broadhurst, T., Wong, J., et al. 2016, *MNRAS*, **459**, 3447
- Diego, J. M., Tegmark, M., Protopapas, P., & Sandvik, H. B. 2007, *MNRAS*, **375**, 958
- Diehl, H. T., Allam, S. S., Annis, J., et al. 2009, *ApJ*, **707**, 686
- Duffy, A. R., Schaye, J., Kay, S. T., & Dalla Vecchia, C. 2008, *MNRAS*, **390**, L64
- Ebeling, H., Ma, C. J., Kneib, J. P., et al. 2009, *MNRAS*, **395**, 1213
- Ebeling, H., Qi, J., & Richard, J. 2017, *MNRAS*, **471**, 3305

- Elíasdóttir, Á., Limousin, M., Richard, J., et al. 2007, arXiv e-prints, arXiv:0710.5636
- Evrard, A. E., MacFarland, T. J., Couchman, H. M. P., et al. 2002, *ApJ*, **573**, 7
- Gladders, M. D., & Yee, H. K. C. 2000, *AJ*, **120**, 2148
- Gonzalez, A. H., Stanford, S. A., Brodwin, M., et al. 2012, *ApJ*, **753**, 163
- Gralla, M. B., Sharon, K., Gladders, M. D., et al. 2011, *ApJ*, **737**, 74
- Graur, O., Rodney, S. A., Maoz, D., et al. 2014, *ApJ*, **783**, 28
- Halkola, A., Hildebrandt, H., Schrabback, T., et al. 2008, *A&A*, **481**, 65
- Heitmann, K., Finkel, H., Pope, A., et al. 2019, *ApJS*, **245**, 16
- Hennawi, J. F., Gladders, M. D., Oguri, M., et al. 2008, *AJ*, **135**, 664
- Hsu, L.-Y., Ebeling, H., & Richard, J. 2013, *MNRAS*, **429**, 833
- Huang, K.-H., Lemaux, B. C., Schmidt, K. B., et al. 2016, *ApJL*, **823**, L14
- Huang, X., Storfer, C., Gu, A., et al. 2021, *ApJ*, **909**, 27
- Huterer, D., & Shafer, D. L. 2018, *Reports on Progress in Physics*, **81**, 016901
- Ishigaki, M., Kawamata, R., Ouchi, M., et al. 2015, *ApJ*, **799**, 12
- Jauzac, M., Richard, J., Jullo, E., et al. 2015, *MNRAS*, **452**, 1437
- Jauzac, M., Richard, J., Limousin, M., et al. 2016, *MNRAS*, **457**, 2029
- Johnson, T. L., Sharon, K., Bayliss, M. B., et al. 2014, *ApJ*, **797**, 48
- Johnson, T. L., Sharon, K., Gladders, M. D., et al. 2017, *ApJ*, **843**, 78
- Jullo, E., & Kneib, J. P. 2009, *MNRAS*, **395**, 1319
- Jullo, E., Kneib, J. P., Limousin, M., et al. 2007, *New Journal of Physics*, **9**, 447
- Karman, W., Caputi, K. I., Caminha, G. B., et al. 2017, *A&A*, **599**, A28
- Kawamata, R., Ishigaki, M., Shimasaku, K., et al. 2018, *ApJ*, **855**, 4
- Kawamata, R., Oguri, M., Ishigaki, M., Shimasaku, K., & Ouchi, M. 2016, *ApJ*, **819**, 114
- Keeton, C. R. 2011, GRAVLENS: Computational Methods for Gravitational Lensing
- Khedekar, S., & Majumdar, S. 2013, *Journal of Cosmology and Astro-Particle Physics*, **2013**, 030
- Killedar, M., Borgani, S., Fabjan, D., et al. 2018, *MNRAS*, **473**, 1736
- Kneib, J.-P., & Natarajan, P. 2011, *Astronomy and Astrophysics Review*, **19**, 47
- Kochanek, C. S. 2006, Strong Gravitational Lensing (Berlin, Heidelberg: Springer Berlin Heidelberg), 91
- Koester, B. P., Gladders, M. D., Hennawi, J. F., et al. 2010, *ApJL*, **723**, L73
- Komatsu, E., Smith, K. M., Dunkley, J., et al. 2011, *The Astrophysical Journal Supplement Series*, **192**, 18
- Kubo, J. M., Allam, S. S., Drabek, E., et al. 2010, *ApJL*, **724**, L137
- Lagattuta, D. J., Richard, J., Bauer, F. E., et al. 2019, *MNRAS*, **485**, 3738
- Liesenborgs, J., De Rijcke, S., & Dejonghe, H. 2006, *MNRAS*, **367**, 1209
- Limousin, M., Ebeling, H., Ma, C. J., et al. 2010, *MNRAS*, **405**, 777
- Limousin, M., Richard, J., Jullo, E., et al. 2016, *A&A*, **588**, A99
- Lotz, J. M., Koekemoer, A., Coe, D., et al. 2017, *ApJ*, **837**, 97
- LSST Science Collaboration, Marshall, P., Anguita, T., et al. 2017, ArXiv e-prints, arXiv:1708.04058
- Mahler, G., Richard, J., Clément, B., et al. 2018, *MNRAS*, **473**, 663
- Mahler, G., Sharon, K., Fox, C., et al. 2019, *ApJ*, **873**, 96
- Mainali, R., Stark, D. P., Tang, M., et al. 2020, *MNRAS*, **494**, 719
- Mantz, A. B., Allen, S. W., Morris, R. G., et al. 2014, *MNRAS*, **440**, 2077
- McCully, C., Keeton, C. R., Wong, K. C., & Zabludoff, A. I. 2014, *MNRAS*, **443**, 3631
- Meneghetti, M., Bartelmann, M., Dahle, H., & Limousin, M. 2013, *SSRv*, **177**, 31
- Meneghetti, M., Rasia, E., Merten, J., et al. 2010, *A&A*, **514**, A93
- Meneghetti, M., Rasia, E., Vega, J., et al. 2014, *ApJ*, **797**, 34
- Meneghetti, M., Natarajan, P., Coe, D., et al. 2017, *MNRAS*, **472**, 3177
- Merten, J., Meneghetti, M., Postman, M., et al. 2015, *ApJ*, **806**, 4
- Mohammed, I., Liesenborgs, J., Saha, P., & Williams, L. L. R. 2014, *MNRAS*, **439**, 2651
- Morgan, R., Nord, B., Birrer, S., Lin, J., & Poh, J. 2021, *The Journal of Open Source Software*, **6**, 2854
- Narayan, R., & Bartelmann, M. 1996, ArXiv e-prints, astro
- Newman, A. B., Treu, T., Ellis, R. S., & Sand, D. J. 2011, *ApJL*, **728**, L39
- Newman, A. B., Treu, T., Ellis, R. S., et al. 2013, *ApJ*, **765**, 24

- Niemiec, A., Jauzac, M., Jullo, E., et al. 2020, *MNRAS*, **493**, 3331
- Ofek, E. O., Seitz, S., & Klein, F. 2008, *MNRAS*, **389**, 311
- Oguri, M. 2010, glafic: Software Package for Analyzing Gravitational Lensing
- Oguri, M., Bayliss, M. B., Dahle, H., et al. 2012, *MNRAS*, **420**, 3213
- Paterno-Mahler, R., Sharon, K., Coe, D., et al. 2018, *ApJ*, **863**, 154
- Pearson, J., Li, N., & Dye, S. 2019, *MNRAS*, **488**, 991
- Pillepich, A., Reiprich, T. H., Porciani, C., Borm, K., & Merloni, A. 2018, *MNRAS*, **481**, 613
- Planck Collaboration, Ade, P. A. R., Aghanim, N., et al. 2016, *A&A*, **594**, A27
- Postman, M., Coe, D., Benítez, N., et al. 2012, *ApJS*, **199**, 25
- Pratt, G. W., Arnaud, M., Biviano, A., et al. 2019, *SSRv*, **215**, 25
- Priewe, J., Williams, L. L. R., Liesenborgs, J., Coe, D., & Rodney, S. A. 2017, *MNRAS*, **465**, 1030
- Raney, C. A., Keeton, C. R., & Brennan, S. 2020a, *MNRAS*, **492**, 503
- Raney, C. A., Keeton, C. R., Brennan, S., & Fan, H. 2020b, *MNRAS*, **494**, 4771
- Ravindranath, S., & Ho, L. C. 2002, *ApJ*, **577**, 133
- Remolina González, J. D., Sharon, K., Li, N., et al. 2021, *ApJ*, **910**, 146
- Remolina González, J. D., Sharon, K., & Mahler, G. 2018, *ApJ*, **863**, 60
- Remolina González, J. D., Sharon, K., Reed, B., et al. 2020, *ApJ*, **902**, 44
- Richard, J., Kneib, J.-P., Ebeling, H., et al. 2011, *MNRAS*, **414**, L31
- Richard, J., Claeysens, A., Lagattuta, D. J., et al. 2020, arXiv e-prints, arXiv:2009.09784
- Rigby, J. R., Bayliss, M. B., Sharon, K., et al. 2018, *AJ*, **155**, 104
- Salmon, B., Coe, D., Bradley, L., et al. 2018, *ApJL*, **864**, L22
- . 2020, *ApJ*, **889**, 189
- Schneider, P. 2006, Introduction to Gravitational Lensing and Cosmology (Berlin, Heidelberg: Springer Berlin Heidelberg), 1
- Sebesta, K., Williams, L. L. R., Liesenborgs, J., Medezinski, E., & Okabe, N. 2019, *MNRAS*, **488**, 3251
- Sharon, K., Gladders, M. D., Rigby, J. R., et al. 2012, *ApJ*, **746**, 161
- Sharon, K., Bayliss, M. B., Dahle, H., et al. 2017, *ApJ*, **835**, 5
- . 2020, *ApJS*, **247**, 12
- Shin, T., Adhikari, S., Baxter, E. J., et al. 2019, *MNRAS*, **487**, 2900
- Smith, G. P., Kneib, J.-P., Ebeling, H., Czoske, O., & Smail, I. 2001, *ApJ*, **552**, 493
- Smith, G. P., Kneib, J.-P., Smail, I., et al. 2005, *MNRAS*, **359**, 417
- Stark, D. P., Auger, M., Belokurov, V., et al. 2013, *MNRAS*, **436**, 1040
- Strait, V., Bradač, M., Hoag, A., et al. 2018, *ApJ*, **868**, 129
- Strait, V., Bradač, M., Coe, D., et al. 2020, *ApJ*, **888**, 124
- Sunyaev, R. A., & Zeldovich, Y. B. 1970, *Ap&SS*, **7**, 3
- Umetsu, K., & Diemer, B. 2017, *ApJ*, **836**, 231
- Vega-Ferrero, J., Diego, J. M., & Bernstein, G. M. 2019, *MNRAS*, **486**, 5414
- Zitrin, A., Broadhurst, T., Umetsu, K., et al. 2009, *MNRAS*, **396**, 1985
- Zitrin, A., Rosati, P., Nonino, M., et al. 2012, *ApJ*, **749**, 97
- Zitrin, A., Zheng, W., Broadhurst, T., et al. 2014, *ApJL*, **793**, L12
- Zitrin, A., Fabris, A., Merten, J., et al. 2015, *ApJ*, **801**, 44